Supporting Information for

Photochemically-assisted Synthesis of Birnessite Nanosheets and Their Structural Alteration in the Presence of Pyrophosphate

Haesung Jung, Tandeep S. Chadha, Yujia Min, Pratim Biswas, and Young-Shin Jun*

Department of Energy, Environmental and Chemical Engineering, Washington University, St. Louis, Missouri, 63130, United States

Address: One Brookings Drive, Campus Box 1180

E-mail: ysjun@seas.wustl.edu

Phone: (314)935-4539

Fax: (314)935-7211

http://encl.engineering.wustl.edu/

*To Whom Correspondence Should be Addressed

Summary: Thirteen pages, including analytical description and eight Figures and three Tables

Small angle X-ray scattering analyses. The 1D intensity profiles in Figure 3A were analyzed by eqn (1) and (2):[1-3]

$$I(q) = NP(q,r,\sigma)S(q,I_{pow},d,R_h,v_f), \quad (1)$$

$$S(q,I_{pow},d,R_h,v_f) = I_{pow}q^{-\mu} + S(q,R_h,v_f). \quad (2)$$

Here, N is the number density, $P(q, r, \sigma)$ is the particle form factor, q is the scattering vector, r is the radius, σ is the standard deviation, and $S(q, I_{pow}, \mu, R_h, v_f)$ is the structural factor. For the particle form factor, we considered the polydisperse size distribution of particles using the Schultz distribution in our systems. Two separate terms, for aggregates ($I_{pow}q^{-\mu}$) and primary particles ($S(q, R_h, v_f)$), describe the structural factor. $I_{pow}q^{-\mu}$ explains the fractal behavior of aggregates of primary particles.[4-5] $S(q, R_h, v_f)$ represents the hard-sphere Percus-Yevick model, with R_h and v_f being the hard-sphere interaction distance and volume fraction, respectively. For dilute systems, the structure factor is equal to one.[2] Fitted values of r and σ under varied pyrophosphate concentrations were used to calculate the radii of gyration (R_g) of the thickness of δ-MnO_2 nanosheets, according to the Schultz distribution function:

$$R_g = \mu_R\sqrt{\frac{3(z+8)(z+7)}{5(z+1)^2}}. \quad (3)$$

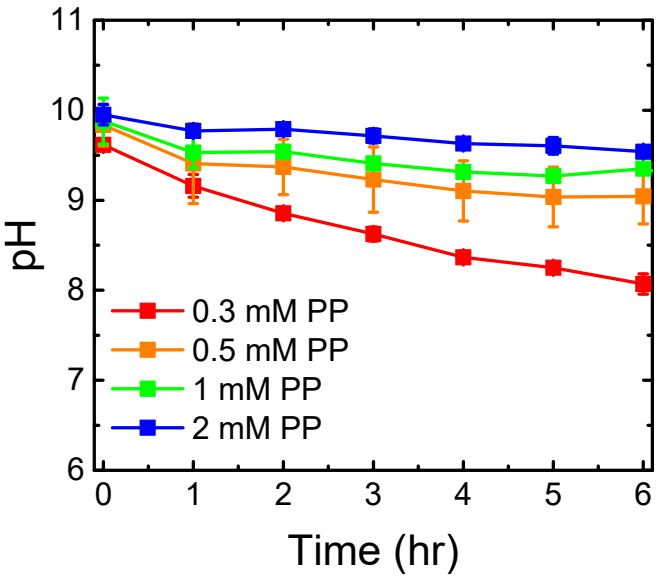

Figure S1. pH measurements during photochemically-assisted oxidation and formation of δ-MnO_2 nanosheets under various PP concentrations with time lapses. The quite consistent pH conditions resulted from the buffering capability of pyrophosphate. Because 0.3 mM PP is a relatively lower concentration than the others, the pH decreased from 9.6 to 8.1 after 6 hrs. Other conditions showed pH decreases less than 1 over 6 hrs.

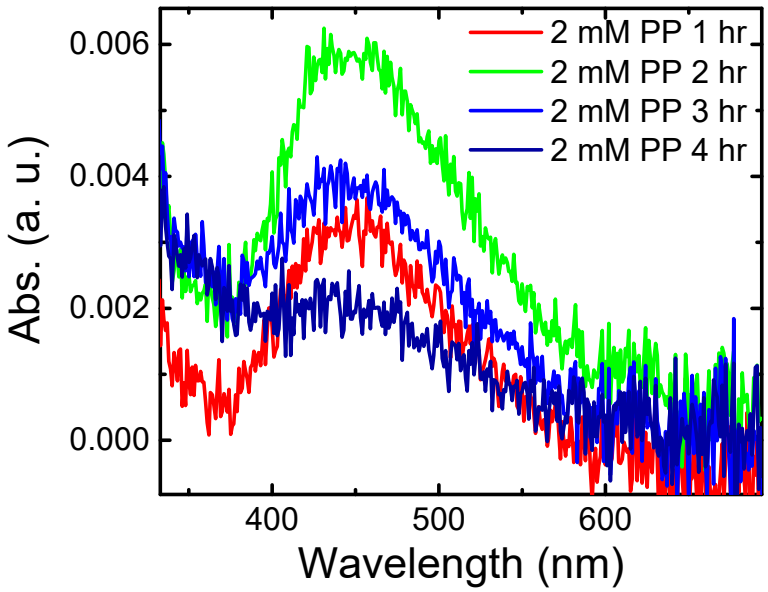

Figure S2. The absorption spectra of Mn(III)-PP under the photochemical oxidation at 2 mM PP. The absorption peaks were placed at ~445 nm without any shift, which indicates that there is no any change in the property of complexation, such as protonation or deprotonation.[6]

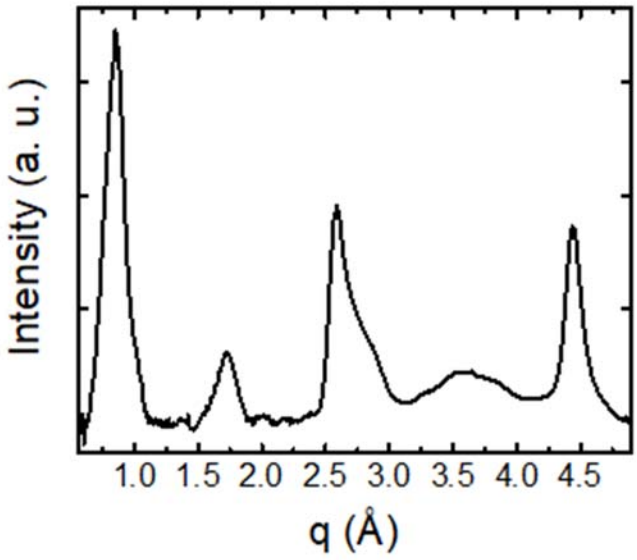

Figure S3. Synchrotron-based wide angle X-ray scattering of layered birnessite nanosheets synthesized from the nitrate photolysis without PP.

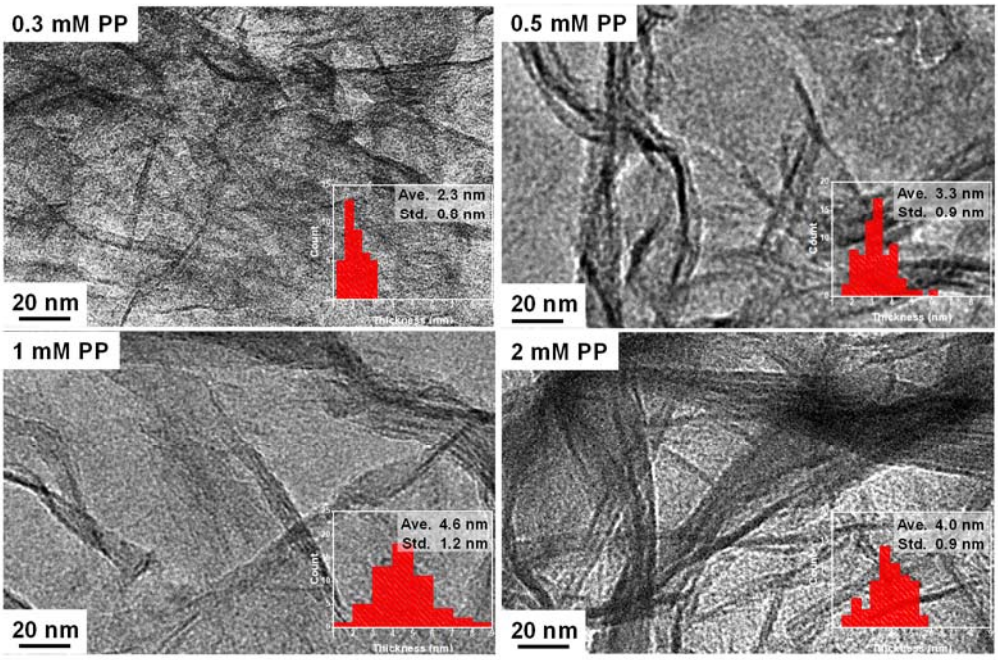

Figure S4. TEM images under various PP concentrations, with the distribution of thicknesses shown in the insets. TEM images show a consistent trend of thickness increase with the increase of PP, as also observed in the SAXS fitting results. The analyzed thickness from TEM also shows that the thickness at 1 mM PP is slightly thicker than that at 2 mM PP, which supports the consistency of the SAXS fitting results with the TEM analysis.

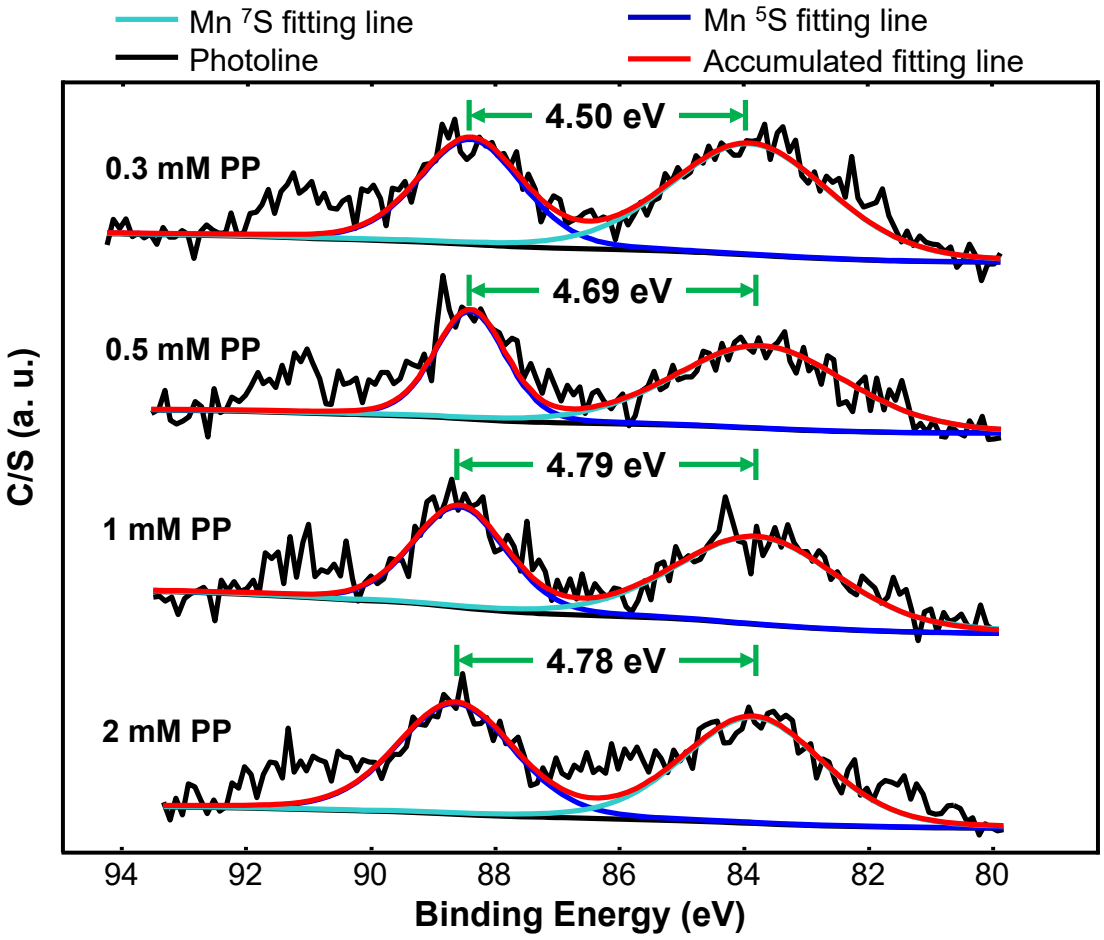

Figure S5. Energy gap of Mn 3s (ΔE_{Mn3s}) from XPS spectra under varied PP concentrations. Mn ^{7}s and Mn ^{5}s occur at ~89 eV and ~84 eV, respectively, and the energy gap of Mn 3s is variable between ~4.5 eV to ~ 6 eV depending on the oxidation state of Mn. The increase in the energy gap from ~4.5 eV to ~4.8 eV with the increase of PP concentration indicates a lower oxidation state due to a larger portion of Mn(III) in the Mn oxide layers.

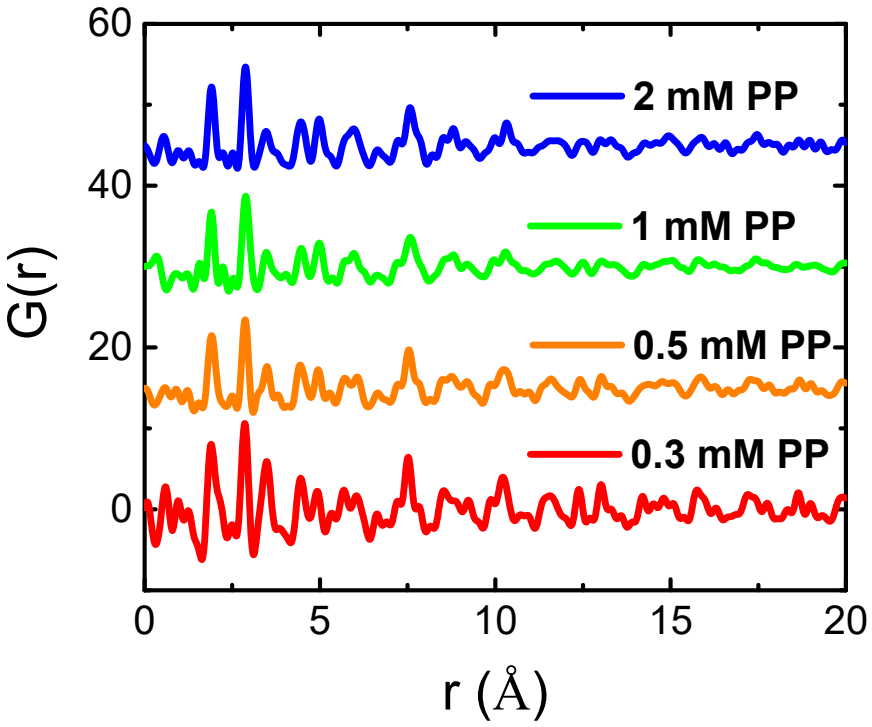

Figure S6. Pair distribution functions (G(r)) under the varied PP concentrations.

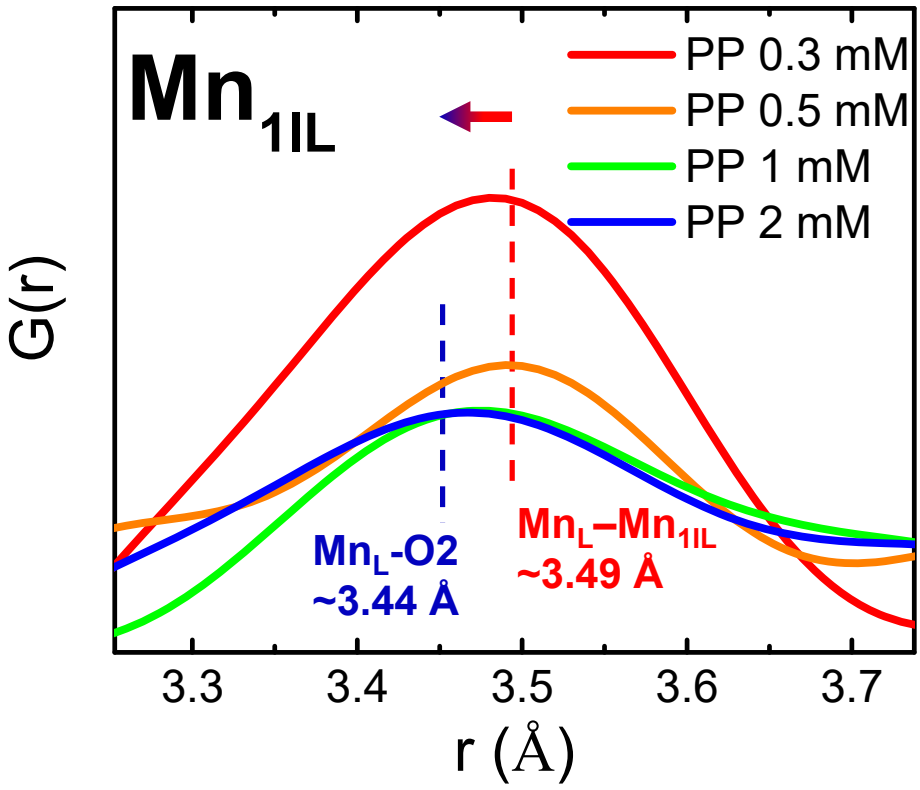

Figure S7. Correlation of the shift of Mn–O2 (~3.44 Å) to Mn_L–Mn_{1IL} (~3.49 Å) in the presence of interlayer Mn(III) under 0.3 and 0.5 mM PP. Specifically, the peak shift occurred most significantly in 0.5 mM PP, r = ~3.49 Å, which indicates the largest portion of interlayer Mn(III) is in 0.5 mM PP. Because Mn(III) is mostly placed in layers, not in interlayers under 1 and 2 mM, the PDF shows the Mn–O2 peak at around 3.44 Å.

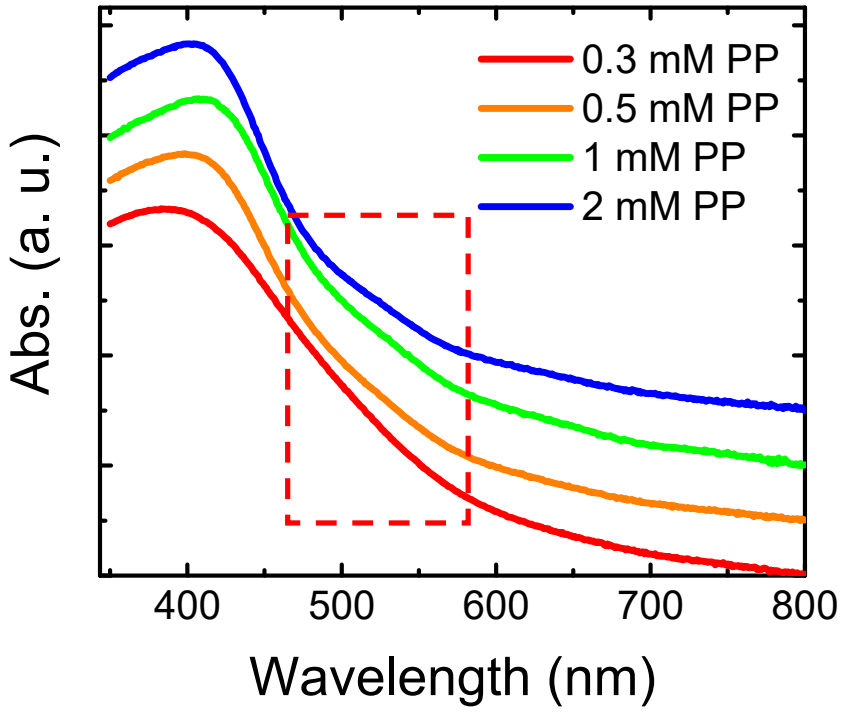

Figure S8. The emerge of the absorbance peak of reactive Mn(III) for water oxidation catalysis at ~510 nm. The higher the PP concentration, the stronger the absorbance peak. The absorbance spectra indicate that reactive Mn(III) is not necessarily related only to interlayer Mn(III). Note the weaker absorbance at 0.5 mM PP, which has the largest portion of interlayer Mn(III), compared to those at 1 and 2 mM PP. The reactive Mn(III) might relate to Mn(III) in layers or to the fraction of total Mn(III) in the structures.

Table S1. Chemical compositions of the δ-MnO_2 nanosheets under various PP concentrations.

	Na/Mn (mol %)	Water percentage (mass %)	Chemical compositions
0.3 mM PP	0.005 ± 0.003	13.0	$MnO_2 \cdot 0.72H_2O$
0.5 mM PP	0.012 ± 0.008	11.6	$Na_{0.01}MnO_2 \cdot 0.64H_2O$
1 mM PP	0.042 ± 0.004	12.9	$Na_{0.04}MnO_2 \cdot 0.71H_2O$
2 mM PP	0.097 ± 0.012	11.2	$Na_{0.1}MnO_2 \cdot 0.62H_2O$

Table S2. Hydrodynamic particle sizes under various PP concentrations after 6 hr reactions, analyzed by dynamic light scattering.

	0.3 mM PP	0.5 mM PP	1 mM PP	2 mM PP
Number mean particle size (nm)	578 ± 25	731 ± 52	828 ± 78	948 ± 98

Table S3. Summary of XPS references for Mn(II), Mn(III), and Mn(IV).

Oxidation state	Mn oxide	Mn $2p_{3/2}$ Binding energy (eV)	ΔE3s	References
Mn(II)	MnO	640.8	5.8	Junta and Hochella (1994) [7]
	MnO	641.0	6.1	Di Castro and Polzonetti (1989) [8]
	MnO	-	6.0	Gorlin and Jaramillo (2010) [9]
Mn(III)	Mn_2O_3	641.9	5.2	Di Castro and Polzonetti (1989) [8]
	Mn_2O_3	641.8	5.0	Ramesh et al. (2008) [10]
	Mn_2O_3	-	5.1	Gorlin and Jaramillo (2010) [9]
	γ-MnOOH	641.7	5.4	Junta and Hochella (1994) [7]
	γ-MnOOH	641.7	5.4	Jung and Jun (2016) [11]
Mn(IV)	MnO_2	642.2	4.7	Oku et al. (1975) [12]
	MnO_2	642.3	4.5	Ramesh et al. (2008) [10]
	MnO_2	-	4.5	Gorlin and Jaramillo (2010) [9]
	MnO_2	-	4.5	Pinaud et al. (2011) [13]
	MnO_2	642.0	4.5	Junta and Hochella (1994) [7]

Supporting references

1. Jun, Y.-S.; Lee, B.; Waychunas, G. A., In situ observations of nanoparticle early development kinetics at mineral− water interfaces. *Environ. Sci. Technol.* **2010,** *44* (21), 8182-8189, DOI: 10.1021/es101491e.
2. Li, Q.; Fernandez-Martinez, A.; Lee, B.; Waychunas, G. A.; Jun, Y.-S., Interfacial Energies for Heterogeneous Nucleation of Calcium Carbonate on Mica and Quartz. *Environ. Sci. Technol.* **2014,** *48* (10), 5745-5753, DOI: 10.1021/es405141j
3. Jung, H.; Lee, B.; Jun, Y.-S., Structural Match of Heterogeneously Nucleated $Mn(OH)_2$ (s) Nanoparticles on Quartz under Various pH Conditions. *Langmuir* **2016,** *32* (41), 10735-10743, DOI: 10.1021/acs.langmuir.6b02446.
4. Teixeira, J., Small-angle scattering by fractal systems. *J. Appl. Crystallogr.* **1988,** *21* (6), 781-785, DOI: 10.1107/S0021889888000263.
5. Liao, H.-C.; Tsao, C.-S.; Shao, Y.-T.; Chang, S.-Y.; Huang, Y.-C.; Chuang, C.-M.; Lin, T.-H.; Chen, C.-Y.; Su, C.-J.; Jeng, U. S.; Chen, Y.-F.; Su, W.-F., Bi-hierarchical nanostructures of donor–acceptor copolymer and fullerene for high efficient bulk heterojunction solar cells. *Energy Environ. Sci.* **2013,** *6* (6), 1938-1948, DOI: 10.1039/c3ee24312e.
6. Bozor, I.; Simándi, L. I., Oxidation of tiron by (pyrophosphato) manganese (III). Kinetics and mechanism. *Dalton Trans.* **2002,** (16), 3226-3233, DOI: 10.1039/B204678D.
7. Junta, J. L.; Hochella Jr, M. F., Manganese (II) oxidation at mineral surfaces: A microscopic and spectroscopic study. *Geochim. Cosmochim. Acta* **1994,** *58* (22), 4985-4999, DOI: 10.1016/0016-7037(94)90226-7
8. Di Castro, V.; Polzonetti, G., XPS study of MnO oxidation. *J. Electron Spectrosc. Relat. Phenom.* **1989,** *48* (1), 117-123, DOI: 10.1016/0368-2048(89)80009-X.
9. Gorlin, Y.; Jaramillo, T. F., A Bifunctional Nonprecious Metal Catalyst for Oxygen Reduction and Water Oxidation. *J. Am. Chem. Soc.* **2010,** *132* (39), 13612-13614, DOI: 10.1021/ja104587v.
10. Ramesh, K.; Chen, L.; Chen, F.; Liu, Y.; Wang, Z.; Han, Y.-F., Re-investigating the CO oxidation mechanism over unsupported MnO, Mn_2O_3 and MnO_2 catalysts. *Catal. Today* **2008,** *131* (1), 477-482, DOI: 10.1016/j.cattod.2007.10.061.
11. Jung, H.; Jun, Y.-S., Ionic Strength-Controlled Mn (Hydr)oxide Nanoparticle Nucleation on Quartz: Effect of Aqueous $Mn(OH)_2$. *Environ. Sci. Technol.* **2016,** *50* (1), 105-113, DOI: 10.1021/acs.est.5b02819.
12. Oku, M.; Hirokawa, K.; Ikeda, S., X-ray photoelectron spectroscopy of manganese—oxygen systems. *J. Electron Spectrosc. Relat. Phenom.* **1975,** *7* (5), 465-473, DOI: 10.1016/0368-2048(75)85010-9.
13. Pinaud, B. A.; Chen, Z.; Abram, D. N.; Jaramillo, T. F., Thin Films of Sodium Birnessite-Type MnO_2: Optical Properties, Electronic Band Structure, and Solar Photoelectrochemistry. *J. Phys. Chem. C* **2011,** *115* (23), 11830-11838, DOI: 10.1021/jp200015p.